Journal of The Electrochemical Society, 2022 **169** 100522
1945-7111/2022/169(10)/100522/15/$40.00 © 2022 The Authors. Published on behalf of ECS by IOP Publishing Limited

Investigating the Effects of Operation Variables on All-Vanadium Redox Flow Batteries Through an Advanced Unit-Cell Model

Vanesa Muñoz-Perales,[1] Sabrina Berling,[2] Enrique García-Quismondo,[2] Pablo A. García-Salaberri,[1] Jesús Palma,[2] Marcos Vera,[1] and Santiago E. Ibáñez[2,z]

[1]*Departamento de Ingeniería Térmica y de Fluidos, Universidad Carlos III de Madrid, Avda. de la Universidad 30, 28911, Leganés, Spain*
[2]*Electrochemical Processes Unit, IMDEA Energy, Avda. Ramón de la Sagra 3, 28935 Móstoles, Spain*

Next-generation redox flow batteries will benefit from the progress of macroscopic continuum models that enable the optimization of new architectures without the need of expensive fabrication and experimentation. Despite previous attempts, there is still need for robust and thoroughly validated models. Here, a steady-state two-dimensional unit-cell model of an all-vanadium redox flow battery is presented. The model integrates state-of-the-art descriptions of the fundamental physical phenomena, along with new features such as local mass transfer coefficients for each active species, precise sulfuric acid dissociation kinetics, and experimental data of the electrochemical parameters and electrolyte properties. The model is validated at different states of charge and flow rates using polarization, conductivity and open circuit voltage measurements. Then, the contribution of operating conditions on battery performance is studied by analyzing its separate effect on the various phenomena that affect cell performance, such as local pore mass transfer limitations, parasitic hydrogen evolution reactions, crossover and self-discharge fluxes. The resulting model is a reliable tool that can be used to assess the relevance of these coupled phenomena that take place simultaneously within the reaction cell. This important information is critical to optimize cell components, reactor design and to select optimal operating conditions.
 [DOI: 10.1149/1945-7111/ac975f]

Manuscript submitted March 29, 2022; revised manuscript received August 16, 2022. Published October 18, 2022.

List of symbols

Symbols

a	electrode specific surface area, $m^2\ m^{-3}$
C	concentration, mol m^{-3}
d_f	carbon electrode fiber diameter, m
D_i	diffusion coefficient of species i, $m^2\ s$
D	depth measured along z-direction, m
E'	formal potential, V
E_{eq}	equilibrium potential, V
F	Faraday constant, 96,487 C mol^{-1}
i	current density, A m^{-2}
i_0	exchange current density, A m^{-2}
k	reaction rate constant, m s^{-1}
k_b	backward rate constant of the HSO_4^- dissociation reaction, s^{-1}
k_f	forward rate constant of the HSO_4^- dissociation reaction, s^{-1}
k_m	mass transfer coefficient, m s^{-1}
K_{eq}	corrected equilibrium constant for the bisulfate ion dissociation reaction, M
L	length measured along y-direction, m
M	mass, m
N	molar flux, mol $m^{-2}s^{-1}$
Q_v	volume flow rate, $m^3\ s^{-1}$
R	universal gas constant, 8.314 J $mol^{-1}K^{-1}$
T	temperature, K
u	liquid velocity, m s^{-1}
U	ion mobility, mol $s^{-1}kg^{-1}$
W	width measured along x-direction, m
$W_{L,V}$	volumetric electrolyte uptake, dimensionless
z	charge number of the ionic species

Greek symbols

β	degree of dissociation, dimensionless
α_k	transfer coefficient, $k = \{a,\ c,\ H_2,\ O_2\}$, dimensionless
ϵ	porosity, dimensionless
η	overpotential, V
ϕ	potential, V
η	electrolyte conductivity, S m^{-1}
ξ	flux from self-discharge reactions, mol $m^{-2}\ s^{-1}$
Ψ	net flux, mol $m^{-2}\ s^{-1}$
γ	activity ratio
μ	dynamic viscosity, cP
ρ	density, g cm^{-3}
ν	stoichiometric coefficients, dimensionless

Subscripts

a	anode
a_k	viscosity fitting coefficients, $k = \{0,...,3\}$
b_k	density fitting coefficients $k = \{0,...,2\}$
c	cathode
e	solid electrode domain
eq	equilibrium
i	V^{2+}, V^{3+}, VO^{2+}, VO_2^+, H^+, HSO_4^-, SO_4^{2-}, H_2 and O_2 species
in	inlet value
j	vanadium species V^{2+}, V^{3+}, VO^{2+}, VO_2^+
L	electrolyte domain
O	oxidized species
R	reduced species
S	sulfates
V_T	total vanadium

Superscripts

eff	effective value
L	electrolyte domain
m	membrane domain
s	surface
*	bulk
0	standard or initial value
−	negative electrode, electrolyte or half-cell
+	positive electrode, electrolyte or half-cell

The current energy scenario is characterized by a continued growth in the penetration of renewable energy sources, which leads to an ever-increasing temporal variability in the power generation

[z]E-mail: santiago.ibanez@imdea.org

capacity of the grid. This fluctuating energy generation must guarantee the electricity supply to a system whose demand also changes with time. A wide mix of energy storage technologies with different capacities and response times is thus crucial to improve the reliability and stability of future smart grids,[1] thereby enhancing the versatility of intermittent renewable energies such as wind and solar.[2] Electrochemical storage systems convert electrical energy into chemical energy by means of redox reactions. In this context, Redox Flow Batteries (RFBs) emerge as a mature and popular technology due to their flexibility to decouple energy from power and wide range of power to energy ratios.[3]

RFBs are a promising technology, particularly well suited for stationary energy storage.[4] They are a type of rechargeable battery that, unlike conventional batteries, do not store energy in the electrodes.[5] RFBs are a variant of regenerative fuel cells that store the energy in the form of redox active species dissolved in two electrolytes that react on the surface of two electrodes separated by a porous separator or membrane.[1] A large body of work has been devoted to increase the overall efficiency of RFBs by testing different electrochemically active species,[5] long lasting and more efficient electrodes,[6–8] more selective and conductive separator materials,[9,10] optimized flow field designs[11,12] and controlled operating conditions.[13–15] The storage of electrolytes in external deposits gives RFBs their unique ability to decouple power and energy. However, the circulation of the electrolytes between the deposits and the cell stacks requires the use of pumps and flow control systems, which increases their capital and operating costs compared to other types of batteries.[3] So far, most of the literature on RFBs has dealt with Vanadium RFBs (VRFBs), one of the earliest redox couples adopted in RFBs due to the reduced effect of cross-contamination in battery long-term performance.[5]

Mathematical modeling is a powerful tool to expedite the research of next-generation RFBs, which will require robust and thoroughly validated models. Despite the variety of modeling approaches,[15–18] macroscopic continuum models are mostly used to study complete unit cells or stacks, where porous materials are treated as homogeneous media with certain effective, or mean, transport properties.[19] They pose an intermediate compromise between more detailed models of the structure of the electrodes (e.g. pore network models) which are prohibitive at full cell scale due to its computational cost, and simple but fast zero-dimensional dynamic models that cannot retain precisely local variations of electrode or electrolyte properties. These continuum models are often used as starting point to examine the scalability of RFBs in industrial applications, as they provide a cost-effective tool to explore coupled phenomena in electrochemical cells and predict overall performance and efficiency.[20]

Fundamental equations for flow batteries are nowadays well known.[21,22] In these models, it is common to assume steady operation within the cell whenever its inner volume is small compared to the total volume of electrolyte of the system. These steady-state models of the reaction cell can be used to analyze local values of the concentration of species, electrode overpotentials and transfer current densities.[18,23,24] Moreover, they can be extended into system level models if the dynamic response wants to be evaluated over time.[20,25–28]

Current efforts are focused on assessing the importance of the diverse physical phenomena that take place within the cells. Knehr and Kumbur[29] demonstrated that the equilibrium potential of the electrochemical system needs to be properly estimated for an accurate prediction of the cell voltage. Further improvements in the physics description have also been addressed. For instance, the crossover of vanadium species through the membrane of VRFBs is one of the main reasons of their capacity fade. Tang et al.[30] and Oh et al.[31] studied the transport of active species across the membrane and the subsequent capacity loss using a dynamic model based on species mass balances coupled to the Nernst equation, and on the 3D description of the different transport mechanisms, respectively. They reported that the main reasons for electrolyte imbalance between the negative and positive sides are the different diffusion rates and significant migration rates of the active species across the membrane. More recently, using a similar modeling approach, Hao et al.[32] found that it exists an asymmetric behavior in the crossover of vanadium ions which results in ions accumulation in the negative or positive side depending on whether cation or anion exchange membranes are used, respectively.

Models accounting for local variations of electrolyte properties have proven to be remarkably effective in providing more realistic predictions of system performance and pumping losses.[33] Knehr et al.[26] observed that variations in electrolyte viscosity could also impact significantly on species crossover. Additionally, Zhou et al.[34] developed a model including variable diffusion coefficients that depended on electrolyte viscosity, and showed that this in fact leads to a more accurate prediction of the electrolyte ionic conductivity. Other authors such as Shah et al.[35] and Al-Fetlawi et al.[36] investigated secondary parasitic reactions through a dynamic model that integrated advanced descriptions of parasitic hydrogen and oxygen evolution reactions. They demonstrated the detrimental impact of these reactions on the battery efficiency and provided some guidelines for its minimization (e.g., high flow rates to minimize mass transport overpotentials). Finally, in the modeling literature, most macroscopic continuum models reported to date use averaged values for the mass transfer coefficients k_m, often only dependent on the bulk electrolyte velocity.[18,24,37,38] Only a few works have reported a more accurate description of pore mass transport losses, considering, e.g., the dependence of k_m on carbon fiber diameter, ion diffusion coefficients or electrolyte properties.[39–42] By contrast, all these authors model species depletion using a constant mass transfer coefficient k_m throughout the entire electrode domain. It is clear that local electrolyte properties play a role in how active species are transported to the electrode surface but locally dependent electrolyte properties are not included in mass transfer coefficient formulations. A more accurate model of the electrode domain can be used that include a detailed microscopic description of the electrode but these type of models cannot be extended to full cell simulation due to its high computational costs.

Despite the advances reported in all previously mentioned models, there is still a lack of comprehensive multiphysics models that are validated experimentally at diverse operating conditions and that include all relevant physical phenomena. Therefore, in this work, we present a robust and validated model that allow us to deconvolute the interplay between all the physico-chemical phenomena, enabling a more accurate prediction of the specific effects of each component properties, reactor design and operating conditions on the system performance. We developed a comprehensive physical model of a unit-cell VRFB that incorporates for the first time a complete description of the sulfuric acid dissociation equilibrium, local mass transfer coefficients as a function of local electrolyte properties for each vanadium species, along with experimentally measured electrochemical kinetic parameters, electrolyte properties and diffusion coefficients, which improves significantly the accuracy of the model. The model is validated with polarization, conductivity and open circuit voltage (OCV) measurements at different states of charge (SOC) and flow rates. Afterwards, the proposed model is used to perform three parametric sweeps varying the cell voltage, the SOC and the flow rate in order to highlight the relative contribution of the different operating variables. Crossover and self-discharge rates, equilibrium ionic concentrations and hydrogen bubble production risk maps are also presented here. This valuable information could guide the design processes and help to identify strategies for cell optimization and scaling toward the industrial environment. This model is a first step toward a more complex system-level model that will allow us to study charge-discharge cycles under different temperature conditions.

Experimental

Materials and setup.—A lab-size (3 cm × 3 cm) filter-press single cell operating in flow-through configuration was used for the flow-cell experiments. A schematic cross-sectional view and an

image of the experimental setup and cell assembly are shown in Figs. 1 and S1, respectively. The internal geometry of the cell allows us to easily compare experiments with simulations by correctly assuming a 2D flow configuration.

Vanadium electrolytes composed of V^{2+}/V^{3+} and VO^{2+}/VO_2^+ redox species dissolved in aqueous sulfuric acid (H_2SO_4), were used for the negative and positive half-cells, respectively. The electrolytes were obtained from the pre-conditioning of the commercial 1.8 M total vanadium electrolyte supplied by Oxkem Limited (UK) and received as a 50:50 mixture of V^{3+}/VO^{2+}, by galvanostatic charge at 30 mA cm^{-2} up to 1.7 V. The electrolytes were stored in two small PET deposits, which were continuously feed with argon to maintain an inert atmosphere. The electrolytes were pumped from the deposits using a peristaltic pump (Masterflex L/S Series) to a custom made reference cell using Nalgene PVC tubing 1/8 ID, passed through the working cell and then returned back to the deposits. A reference cell is used to ensure that the desired SOC is present at the inlet of the working cell by monitoring the open circuit voltage in real time. To minimize crossover effects in the reference cell two membranes were stacked between the two half-cells. Both the reference and the working cell were connected to a Biologic VMP3 multi-channel potentiostat-galvanostat (Biologic, France). Both cells used Sigracell® battery felt GFD-2.5 EA (SGL Carbon) as porous electrodes, with a geometrical surface area of 9 and 1.5 cm^2, respectively. To improve their wettability, the electrodes were pre-treated by thermal oxidation in a carbolite laboratory chamber furnace at 500 °C for 1 h.[43] As current collectors, carbon bipolar foil Sigracell® TF6/PV15 (fluoropolymer 6%, carbon 94%) (SGL Carbon) was used. A Nafion 212 cationic membrane was used to separate both cell compartments, first conditioned by pumping electrolyte through the cell for two hours. Teflon end-plates were used to enclose all the components. A compression ratio of 20% was ensured by keeping a uniform 10 mm separation at the 6 bolt locations. Several layers of vinyl and Teflon sheets served as gaskets for both creating the flow chamber and sealing the cell. The reference cell was made using the same materials as the working cell, but at a smaller scale.

Electrolyte characterization.—Physicochemical and electrochemical properties of the electrolyte were measured in order to feed the model with accurate data. Viscosity, density, pH and electrical conductivity were measured for different electrolyte samples containing a total vanadium concentration of 1.6, 1.8 and 2.0 M and at four different SOCs (10, 20, 50 and 80%) calculated from titration measurements. The data was obtained under controlled temperature (25 °C) inside a climatic chamber. The results are collected in Table S1, with further experimental details discussed in the Suplementary Information. The total concentration of vanadium ions and sulfates present in the electrolyte used in the experiments were measured by ICP-AES technique (see Tables I and SI).

Electrochemical kinetic parameters were studied using two independent techniques. Cyclic voltammetry (CV) was performed using a graphite rod electrode to obtain the formal potential E', the reaction rate constants k^0 and transfer coefficients α of each electrolyte. A rotating disc electrode (RDE) made of glassy carbon was used for diffusion coefficients measurements. Resulting values of these parameters are compiled in Table II. The sum of both negative and positive transfer coefficients of the anodic and cathodic reactions deviates from unity, as also reported in other studies.[45] This can be due to the poor kinetics and to the non-reversible behavior of the vanadium reactions. All experimental details are collected in the Supplementary Information.

Electrolyte uptake in the membrane.—The volumetric electrolyte uptake, $W_{L,V}$, represents the amount of electrolyte inside the wet membrane. This parameter is used later when modeling the membrane to define the fraction of the membrane domain that is in fact occupied by electrolyte. To measure its value, standard practice was followed by immersing the Nafion 212 membrane in electrolyte for 48 h. After that, samples were weighted and then dried inside a vacuum oven at 60 °C during 24 h to be weighted again. Then $W_{L,V}$ was calculated as

$$W_{L,V} = \frac{V_m^L}{V_m}, \qquad [1]$$

where $V_m^L = (M_{wet} - M_{dry})/\rho_L$ is the volume of electrolyte absorbed and $V_m = 1.1 W_m L_m D_m$ is the volume of the wet membrane assuming a 10% swelling.[47] In the above expressions, M_{wet} and M_{dry} represent the mass of the membrane under wet and dry conditions, respectively, ρ_L is the density of the electrolyte, and W_m, L_m and D_m are the initial width, length and depth (in the *x*-, *y*- and *z*-directions in Fig. 1) of the membrane sample used in the experiments. Measured value of $W_{L,V}$ is collected in Table V.

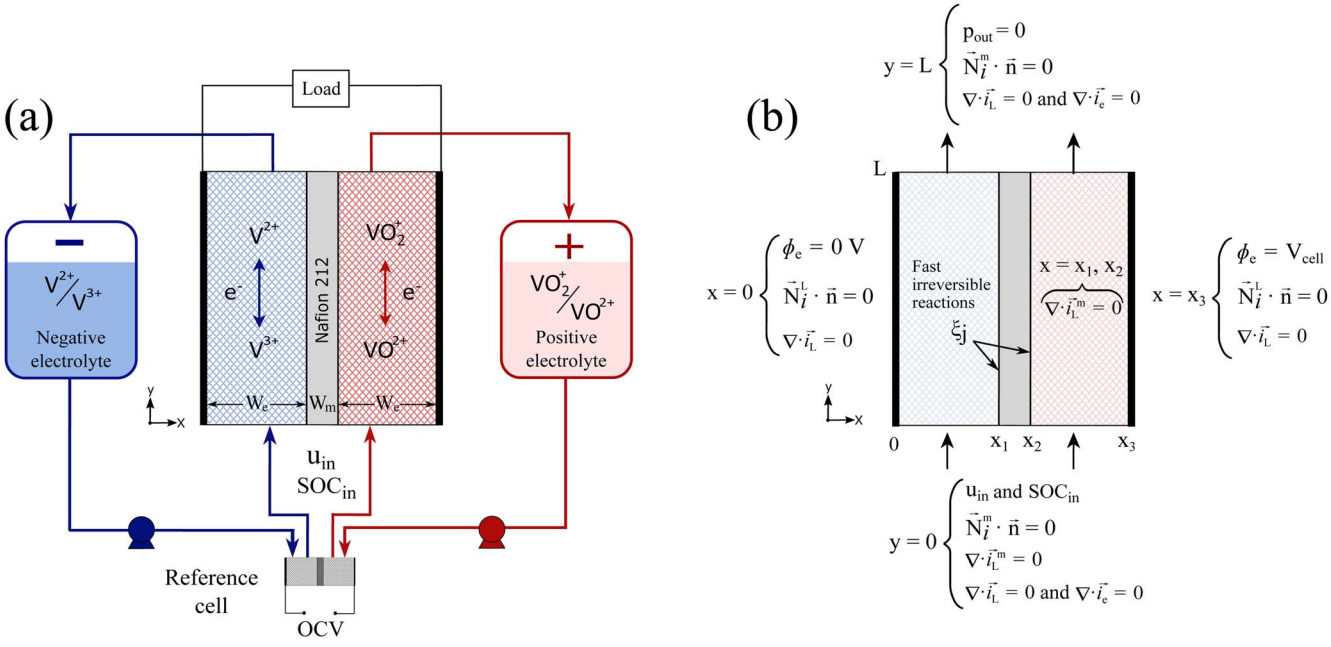

Figure 1. Schematic view of the experimental setup (a) presenting the modeled domain and (b) boundary conditions used in the simulations (see Nomenclature).

Table I. Electrolyte composition.

Symbol	Quantity	Value	Origin
C_{V_T}	Total concentration of vanadium ions (mol m^{-3})	1890	Measured
$C_{sulfates}$	Total concentration of sulfates (mol m^{-3})	3770	Measured
γ	Activity ratio	3.04×10^{-3}	44
K_{eq}	Corrected equilibrium constant	3.74	44
$D^0_{V^{2+}}$	V^{2+} diffusion coefficient (m^2 s^{-1})	8.10×10^{-12}	Measured
$D^0_{V^{3+}}$	V^{3+} diffusion coefficient (m^2 s^{-1})	1.65×10^{-11}	Measured
$D^0_{VO^{2+}}$	VO^{2+} diffusion coefficient (m^2 s^{-1})	2.37×10^{-11}	Measured
$D^0_{VO_2^+}$	VO_2^+ diffusion coefficient (m^2 s^{-1})	4.16×10^{-12}	Measured

Table II. Electrokinetic and electrochemical reactions parameters.

Symbol	Quantity	Value	Origin
E'^-	Formal potential of the negative electrode [V]	−0.36	Measured
E'^+	Formal potential of the positive electrode [V]	+ 0.98	Measured
k^0_-	Standard rate constant of the negative electrode [m s^{-1}]	2.5×10^{-7}	Measured
k^0_+	Standard rate constant of the positive electrode [m s^{-1}]	1.5×10^{-6}	Measured
α_c^-	Cathodic negative reaction transfer coefficient	0.2	Measured
α_a^-	Anodic negative reaction transfer coefficient	0.3	Measured
α_c^+	Cathodic positive reaction transfer coefficient	0.4	Measured
α_a^+	Anodic positive reaction transfer coefficient	0.5	Measured
i_{0,O_2}	Oxygen evolution exchange current density [A m^{-2}]	1.0×10^{-5}	46
i_{0,H_2}	Hydrogen evolution exchange current density [A m^{-2}]	1.4×10^{-5}	35
α_{O_2}	Oxygen evolution transfer coefficient	0.3	46
α_{H_2}	Hydrogen evolution transfer coefficient	0.35	35

Reference cell: open circuit voltage measurement.—The OCV between both electrolytes was continuously monitored in order to estimate the SOC of the electrolyte passing through in real time. The OCV signal was used to control the programmed charge, discharge and relax steps applied to the working cell. The SOC of the battery was extrapolated using a previously calibrated OCV vs SOC curve at the prevailing operating temperature of 25 °C (see the experimental curve in Fig. 2b).

Polarization curves.—Polarization curves were measured at four different flow rates (5, 12, 30 and 50 ml min^{-1}) and four different SOCs (80, 60, 40 and 20%) at 25 °C. Linear sweep voltammetry was selected as a potentiostatic method for the measurements since it allows a smooth voltage variation until the limiting current is reached, providing fast results with a similar accuracy to pulsed voltage techniques. The scan rate of the applied potential was set to a compromise value of 400 mV min^{-1}, sufficiently low to assume stationary conditions inside the cell but fast enough to avoid significant SOC changes. To ensure a stable SOC at the inlets, 90 ml volume of fresh electrolyte was introduced in each side of the working cell. The desired SOC was obtained by charging the battery and discharging at the same current density stopping at the desired SOC levels to measure the corresponding polarization curve. This protocol was repeated for every flow rate with fresh electrolyte in each test.

Mathematical Model

Figure 1 shows a sketch of the two-dimensional unit-cell under study, with dimensions shown in Table III, similar to those used in the 3 cm × 3 cm experimental characterization cell. The positive (+) and negative (−) electrolytes flow in the same direction through two porous electrodes of length $L = 3$ cm and thickness $W_e = 2.5$ mm, separated by a cationic polymer membrane (Nafion 112, see Table V) of thickness $W_m = 50.8$ μm. The domain under study includes the porous electrodes and the membrane, with $0 < x < 2W_e + W_m$ denoting the transverse coordinate measured from the current collector of the negative electrolyte, and $0 < y < L$ the longitudinal coordinate measured from the inlet section. As shown in the figure, $x_1 = W_e$ and $x_2 = W_e + W_m$ correspond to the membrane interfaces with the negative and positive electrodes respectively, while the current collectors are located at the boundaries of the domain $x = 0$ and $x_3 = 2W_e + W_m$. The electrochemical redox reactions occurring at each half-cell are

$$\text{Negative electrode:}\quad V^{3+} + e^- \underset{\text{Discharge}}{\overset{\text{Charge}}{\rightleftharpoons}} V^{2}+ \qquad [2a]$$

$$\text{Positive electrode:}\quad VO^{2+} + H_2O \underset{\text{Discharge}}{\overset{\text{Charge}}{\rightleftharpoons}} VO_2^+ + 2H^+ + e^- \qquad [2b]$$

Following standard practice, the SOC is defined as the ratio of the concentration of charged vanadium ions to the total concentration of vanadium ions in each electrolyte

$$SOC = \frac{C_{V^{2+}}}{C_{V^{2+}} + C_{V^{3+}}} = \frac{C_{VO_2^+}}{C_{VO^{2+}} + C_{VO_2^+}.} \qquad [3]$$

where it is assumed that the electrolyte imbalance is negligible, so that the same SOC and total vanadium concentration are used for both electrolytes at the electrode inlet sections.

The following assumptions have also been considered in the development of the model:

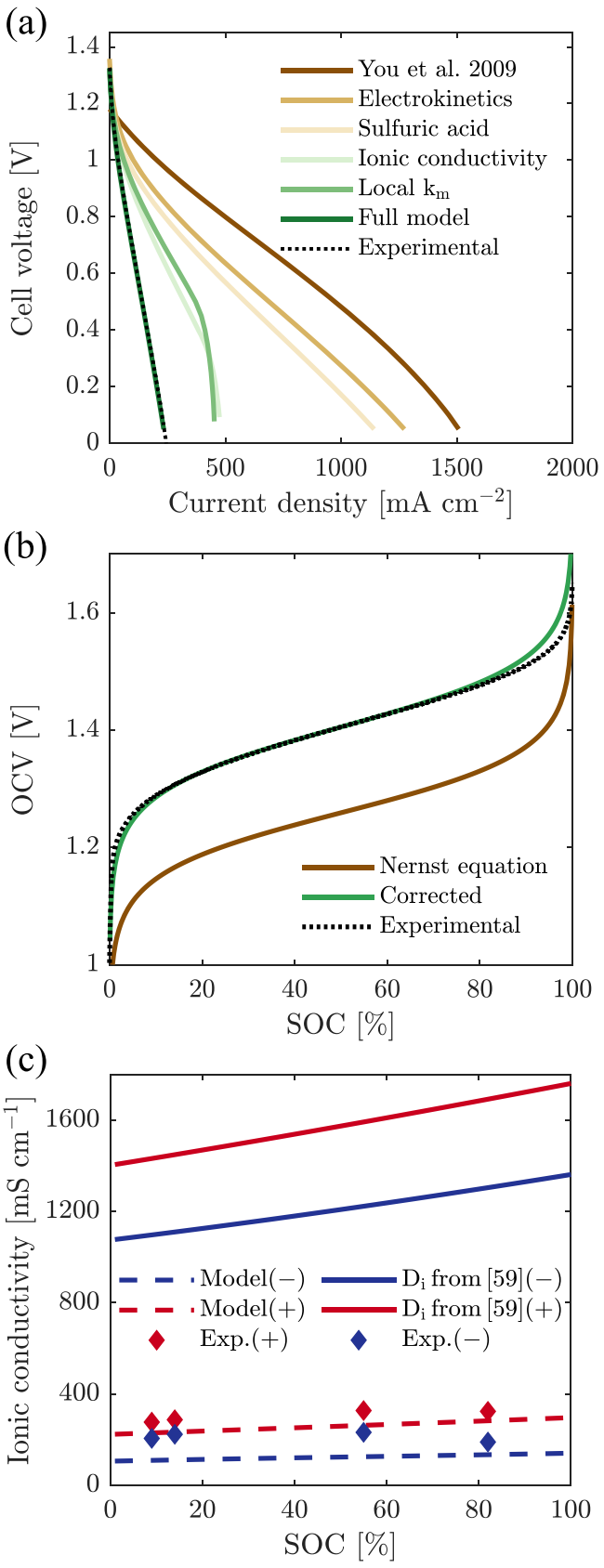

Figure 2. Comparison between numerical results and experiments; (a) Impact of sequential inclusion of different physics in the model in the polarization curve of the battery. $Q_v = 30$ ml min^{-1} and 20% SOC; (b) Open circuit voltage of the cell; and (c) ionic conductivity of each electrolyte, as a function of SOC.

(i) The fluid flow is steady and the effect of buoyancy is negligible.
(ii) The electrolyte velocity is uniform at the electrode inlet section.
(iii) The temperature is uniform throughout the cell.
(iv) The dilute solution approximation holds for all species present in the electrolyte.
(v) Convection and electroosmotic drag are neglected in the membrane.
(vi) Self-discharge reactions are assumed to be instantaneous, irreversible, and only take place at both interfaces between the membrane and the porous electrodes.
(vii) The H_2 and O_2 produced by the hydrogen and oxygen evolution reactions are instantaneously dissolved in the electrolytes.All model equations were implemented in the finite element software COMSOL Multi-physics®. A quadratic mesh with 23 040 elements was used including cell refinement close to the electrode-membrane interface and within the membrane. The relative error tolerance was set to 10^{-5}. The computational time for computing a single point of the polarization curve (e.g., $V_{cell} = 1$ V at 12 ml min^{-1} and 20% SOC) was on the order of 2 min in a AMD Ryzen 9 3900X 12-Core Processor 3.79 GHz CPU supported by 64 GB of RAM.

In the following sections, the model equations are presented and referenced to each of the half-cell domains.

Porous electrodes.—The steady-state species conservation equation in the porous electrodes can be written as

$$\nabla \cdot \vec{N}_i = S_i, \qquad [4]$$

where i refers to the studied species V^{2+}, V^{3+}, VO^{2+}, VO_2^+, H^+, HSO_4^-, SO_4^{2-}, H_2 and O_2. In the above equation, $\vec{N}_i$ is the species molar flux vector and S_i is the volumetric source term of species i that refers to electrochemical production either in the electrode surface or by homogeneous chemical reactions (as defined in Table IV). The molar flux vector includes diffusion, migration and convection terms according to the Nernst-Planck equation

$$\vec{N}_i = -D_i^{\text{eff}} \nabla C_i - \frac{z_i C_i D_i^{\text{eff}}}{RT} F \nabla \phi_L + \vec{u} C_i, \qquad [5]$$

where C_i and z_i are the molar concentration and charge number of species i, F and R are the Faraday and universal gas constants, T is temperature, ϕ_L the electrolyte potential and $D_i^{\text{eff}} = \epsilon^{3/2} D_i$ the effective diffusion coefficient given by the Bruggemann correction.[49] The diffusion coefficient of species i can be expressed in terms of the electrolyte viscosity, μ, which in turn depends on the local SOC, according to Ref. 34

$$D_i = \frac{D_i^0 \mu^0}{\mu}, \qquad [6]$$

where D_i^0 is the diffusion coefficient of each species measured in the electrolyte at the reference viscosity μ^0.

In the convective term of the species flux, $\vec{u}$ refers to the superficial velocity of the electrolyte, calculated from Darcy's law

$$\vec{u} = -\nabla P \frac{K}{\mu}, \qquad [7]$$

where ∇P is the pressure drop and K is the absolute permeability, given by the Carman-Kozeny equation

Table III. Electrode parameters (Sigracell® GFD-2.5 EA).

Symbol	Quantity	Value	Origin
W_e	Thickness (m)	2.5×10^{-3}	Datasheet
L	Lenght (m)	3.0×10^{-2}	Measured
D_e	Depth (m)	3.0×10^{-2}	Measured
Compression	Compression (%)	20	Calculated
ϵ	Open porosity	0.94	Obtained from datasheet
σ_e	Conductivity (S/m)	50	Datasheet
a	Specific surface area ($m^2\ m^{-3}$)	2.3×10^4	Fitting parameter
d_f	Fibre diameter (m)	0.5×10^{-6}	48

$$K = \frac{d_f^2 \varepsilon^3}{K_{CK}(1-\varepsilon)^2} \quad [8]$$

in terms of the average porosity ε and the average fiber diameter d_f of the electrode.

The concentrations of the different species in the electrolyte must satisfy the electro-neutrality condition

$$\sum_i z_i C_i = 0. \quad [9]$$

Moreover, charge conservation allows to couple the ionic current density in the electrolyte, $\vec{i}_L = F\sum_i z_i \vec{N}_i^L$, with the electronic current density in the electrode, $\vec{i}_e = \sigma_e \nabla\phi_e$, which are both related to the local current density i_{loc} at the fibers surface

$$-\nabla\cdot\vec{i}_L = \nabla\cdot\vec{i}_e = a\ i_{loc}. \quad [10]$$

In the above expressions, a is the electrode specific surface area, σ_e the electrical conductivity, and ϕ_e the electric potential of the solid phase. Substituting Eq. 5 in the expression for $\vec{i}_L$ and grouping terms, the ionic conductivity can be expressed as

$$\sigma_L = F^2 \sum z_i^2 U_i C_i \quad [11]$$

where $U_i = D_i/(RT)$ are the mobility coefficients determined from the Nernst-Einstein equation.

The local current density is defined by the Butler-Volmer equation in its concentration-dependent form, which describes the volume-average electrochemical reactions that take place at the fibers surface

$$i_{loc} = i_0\left[\frac{C_R^s}{C_R^*}\exp\left(\frac{\alpha_a F}{RT}\eta\right) - \frac{C_O^s}{C_O^*}\exp\left(-\frac{\alpha_c F}{RT}\eta\right)\right], \quad [12a]$$

where

$$i_0 = Fk^0(C_R^*)^{\alpha_c}(C_O^*)^{\alpha_a} \quad [12b]$$

is the exchange current density, which depends on the standard rate constant of the reaction, k^0, and on the concentrations of the reduced (R) and oxidized (O) species in the bulk of the liquid (*).

The mass transfer flux of vanadium species $j = \{V^{2+}, V^{3+}, VO^{2+}, VO_2^+\}$ across the interface between the electrode and the electrolyte is modeled by assuming a linear Nernst diffusion layer

$$N_j^s = k_{m,j}(C_j^* - C_j^s) = \frac{i_{loc}}{F} \quad [13]$$

Table IV. Volumetric Source terms S_i of species i in Eq. 4.

S_i	Negative electrolyte	Positive electrolyte
V^{2+}	$-ai_{loc}^-/F$	—
V^{3+}	ai_{loc}^-/F	—
VO^{2+}	—	$-ai_{loc}^+/F$
$VO_2{}^+$	—	ai_{loc}^+/F
H^+	$-2ai_{H_2}/F - ai_{loc}^-/F + S_{d,H^+}$	S_{d,H^+}
$HSO_4{}^-$	S_{d,HSO_4^-}	S_{d,HSO_4^-}
SO_4^{2-}	$S_{d,SO_4^{2-}}$	$S_{d,SO_4^{2-}}$
H_2	ai_{H_2}/F	—
O_2	—	ai_{O_2}/F

where C_j^* and C_j^s refers to the species concentrations in the bulk space and at the fibers surface, respectively, and $k_{m,j}$ is the mass transport coefficient of species j. The latter is modeled by the semi-empirical correlation proposed by Deepak et al.[41]

$$k_{m,j} = 7\frac{D_j}{d_f}\mathrm{Re}^{0.4} \quad [14]$$

in terms of the local diffusion coefficient of species j, the average fiber diameter, and the local Reynolds number $\mathrm{Re} = \rho\|\vec{u}\|d_f/\mu$.

Writing the mass transfer relation Eq. 13 for the reduced and oxidized vanadium species, $j = \{R, O\}$, and substituting i_{loc} using Eq. 12 yields a system of two linear equations with two unknowns in each half-cell whose solution provides the species concentrations at the fiber surface, C_j^s, in terms of the species concentrations in the bulk space, C_j^*, and the overall mass transfer coefficients k_{mj} as follows

$$C_O^s = \frac{\left(1+\frac{A}{k_{mR}}\right)C_O^* + \frac{A}{k_{mO}}C_R^*}{1+\frac{A}{k_{mR}}+\frac{B}{k_{mO}}} \quad [15a]$$

$$C_R^s = \frac{\left(1+\frac{B}{k_{mO}}\right)C_R^* + \frac{B}{k_{mR}}C_O^*}{1+\frac{A}{k_{mR}}+\frac{B}{k_{mO}}}, \quad [15b]$$

where the coefficients A and B are given by

$$A = k^0(C_R^*)^{\alpha_c - 1}(C_O^*)^{\alpha_a}\exp\left(\frac{\alpha_a F}{RT}\eta\right) \quad [16a]$$

$$B = k^0 (C_R^*)^{\alpha_c} (C_O^*)^{\alpha_a - 1} \exp\left(\frac{-\alpha_c F}{RT}\eta\right). \quad [16b]$$

The overpotential in each half-cell is defined as

$$\eta = \phi_e - \phi_L - E_{eq}, \quad [17]$$

where the equilibrium potential is given by the corrected Nernst equation,[29] which leads to the following expressions for each electrode

$$E_{eq}^- = E'^- + \frac{RT}{F}\ln\left(\frac{C_{V^{3+}}}{C_{V^{2+}}}\right) \quad [18a]$$

$$E_{eq}^+ = E'^+ + \frac{RT}{F}\ln\left(\frac{C_{VO_2^+}(C_{H^+}^+)^2}{C_{VO^{2+}}}\right), \quad [18b]$$

where E'^- and E'^+ are the (measured) formal potentials of each electrolyte. Although not needed in the mathematical model of the VRFB, the OCV will be used during the validation step. The predicted OCV value can be obtained using the analytical expression

$$OCV = E' + \frac{RT}{F}\ln\left(\frac{C_{V^{2+}} C_{VO_2^+}(C_{H^+}^+)^2 C_{H^+}^+}{C_{V^{3+}} C_{VO^{2+}} C_{H^+}^-}\right) \quad [19]$$

where $E' = E'^+ - E'^-$ is the formal cell potential. In this expression, the Donnan potential, given by Eq. 24 below, has been simplified retaining only the difference between the H^+ concentration in both electrolytes, neglecting the less relevant effect of the remaining species.[29]

Ion-exchange membrane.—Ionic transport in the membrane is modeled for all species except H_2 and O_2 using the charge conservation equation

$$\nabla \cdot \vec{i}_L^{\,m} = 0, \quad [20]$$

where

$$\vec{i}_L^{\,m} = W_{L,V} F \sum_i z_i \vec{N}_i^{\,m} \quad [21]$$

represents the ionic current density in the membrane. An electrolyte-volumetric uptake parameter ($W_{L,V}$) is included to describe the fraction of electrolyte that the membrane uptakes inside its matrix where the ions can be transported (see Table V). This will directly affect the contribution of the membrane to the total ohmic resistance of the battery. The molar flux of the species dissolved in the membrane, $\vec{N}_i^{\,m}$, is modeled according to the Nernst-Planck Eq. 5 neglecting convective and osmotic fluxes

$$\vec{N}_i^{\,m} = -D_i^{\text{eff, m}} \nabla C_i^m - \frac{z_i C_i^m D_i^{\text{eff, m}}}{RT} F \nabla \phi_m \quad [22]$$

where ϕ_m is the potential of the electrolyte fraction contained in the membrane.

The electroneutrality condition in the membrane

$$\sum_i z_i C_i^m + z_f C_f = 0 \quad [23]$$

includes the effect of the fixed sulfonic acid groups present in it, where z_f and C_f denote the charge and concentration of sulfonic groups, respectively.

Finally, the difference between the membrane and electrolyte potentials is given by the Donnan potential

$$\phi_L - \phi_m = \frac{RT}{F}\ln\left(\frac{C_i^L}{C_i^m}\right) \quad [24]$$

which is a function of the concentration of all ionic species in each electrode.[29]

Vanadium electrolytes.— *Physical properties.*—Since viscosity and density undergo variations with the electrolyte composition that may affect the accuracy of the numerical model,[33] empirical correlations are used here for both properties as a function of SOC and the total concentration of vanadium ions (C_{V_T})

$$\mu = a_0 + a_1 SOC + a_2 C_{V_T} + a_3 SOC\, C_{V_T} \quad [25a]$$

$$\rho = b_0 + b_1 SOC + b_2 C_{V_T} \quad [25b]$$

where a_i and b_i are fitting coefficients obtained from the measured properties of our electrolytes (Table SII).

H_2SO_4 dissociation.—The supporting electrolyte (sulfuric acid, H_2SO_4) is known to dissociate into H^+, HSO_4^- and SO_4^{2-} ions according to the following set of reactions

$$H_2SO_4 \longrightarrow H^+ + HSO_4^- \quad [26a]$$

$$HSO_4^- \underset{k_b}{\overset{k_f}{\rightleftharpoons}} H^+ + SO_4^{2-}. \quad [26b]$$

The first dissociation is assumed to be complete since H_2SO_4 is a strong acid with a large equilibrium constant of 2.4×10^6.[52] However, the second dissociation step occurs only partially, following an equilibrium constant that depends on the concentration of H_2SO_4 and on temperature.[44] At equilibrium, the forward and backward reactions, assumed to be first-order reactions, proceed at the same rate

$$k_f C_{HSO_4^-} = k_b C_{H^+} C_{SO_4^{2-}}, \quad [27]$$

where k_f and k_b are the forward and backward reaction rate constants. The equilibrium constant can then be written as

$$K_{eq} = \frac{k_f}{k_b} = \frac{C_{H^+} C_{SO_4^{2-}}}{C_{HSO_4^-}} \quad [28]$$

where K_{eq} is a corrected equilibrium constant calculated dividing the values of K_{eq} reported by Knopf et al.[44] by an activity quotient at different temperatures and total H_2SO_4 concentrations. The influence of the initial H_2SO_4 concentration is not as significant as that of temperature, therefore for the isothermal conditions considered in this work K_{eq} can be assumed to be constant. Its value at 298 K for a total sulfate concentration of 3.77 M is listed in Table I, which is obtained from Knopf et al.[44] by extrapolating to the specific H_2SO_4 concentration considered here.

During normal operation of the battery, protons are produced/consumed electrochemically in the positive electrode and also pass through the cationic membrane modifying the local sulphuric acid equilibrium concentrations. In order to account for these effects additional volumetric source terms must be included in the conservation equations of H^+, HSO_4^- and SO_4^{2-} (see Table IV)

$$S_{d,H^+} = k_f C_{HSO_4^-} - k_b C_{H^+} C_{SO_4^{2-}} \quad [29a]$$

$$S_{d,HSO_4^-} = -k_f C_{HSO_4^-} + k_b C_{H^+} C_{SO_4^{2-}} \quad [29b]$$

Table V. Membrane parameters (Nafion 212).

Symbol	Quantity	Value	Origin
W_m	Thickness (m)	50.8×10^{-6}	Datasheet
$W_{\mathrm{L,V}}$	Volumetric electrolyte uptake	4.8%	Measured
σ_m	Conductivity (S/m)	5.6	50
C_f	Fixed charges (mol/m^3)	1813	Datasheet
$D^m_{H^+}$	H^+ membrane diffusivity (m^2/s)	3.35×10^{-9}	26
$D^m_{HSO_4^-}$	HSO_4^- membrane diffusivity (m^2/s)	4.00×10^{-9}	26
$D^m_{V^{2}+}$	V^2 + membrane diffusivity (m^2/s)	8.77×10^{-12}	51
$D^m_{V^{3}+}$	V^3 + membrane diffusivity (m^2/s)	3.22×10^{-12}	51
$D^m_{VO^{2+}}$	VO^2 + membrane diffusivity (m^2/s)	6.83×10^{-12}	51
$D^m_{VO_2^+}$	VO_2^+ membrane diffusivity (m^2/s)	5.90×10^{-12}	51

$$S_{\mathrm{d},SO_4^{2-}} = k_f C_{HSO_4^-} - k_b C_{H^+} C_{SO_4^{2-}}, \quad [29c]$$

where the value of k_f is set to be large enough to represent a fast response of the dissociation reaction and the value of k_b is obtained afterwards from Eq. 28.

Assuming that electrolytes coming from the deposits are in equilibrium, inlet concentration of all species in are obtained by solving Eqs. 9 and 28, supplemented by the overall balance of sulfate ions

$$C_S = C_{HSO_4^-} + C_{SO_4^{2-}}, \quad [30]$$

where C_S is the (experimentally measured) total concentration of sulfates, which includes HSO_4^- and SO_4^{2-} ions (see Table I).

Side reactions.— *Self-discharge reactions.*—The membrane crossover of vanadium species to the opposite half-cell promotes undesirable self-discharge reactions in the electrolytes bulk.[53,54] In the negative half-cell the side reactions appear as follows

$$VO^{2+} + V^{2+} + 2H^+ \longrightarrow 2V^{3+} + H_2O \quad [31a]$$

$$VO_2^+ + 2V^{2+} + 4H^+ \longrightarrow 3V^{3+} + 2H_2O, \quad [31b]$$

where the reaction between V^{2+} and VO_2^+ is not included as it can be represented by the other remaining two reactions. These reactions are assumed to occur fast and irreversibly, so that they are incorporated in the model as surface source terms at the negative electrode-membrane interface

$$\xi_{V^{2+}} = -N^{\mathrm{m}}_{VO^{2+}} - 2N^{\mathrm{m}}_{VO_2^+} \quad [32a]$$

$$\xi_{V^{3+}} = 2N^{\mathrm{m}}_{VO^{2+}} + 3N^{\mathrm{m}}_{VO_2^+}. \quad [32b]$$

Similarly, in the positive half-cell, the side reactions that take place are

$$V^{2+} + 2VO_2^+ + 2H^+ \longrightarrow 3VO^{2+} + H_2O \quad [33a]$$

$$V^{3+} + VO_2^+ \longrightarrow 2VO^{2+}, \quad [33b]$$

which are also incorporated in the model according to the following surface source terms

$$\xi_{VO^{2+}} = 2N^{\mathrm{m}}_{V^{3+}} + 3N^{\mathrm{m}}_{V^{2+}} \quad [34a]$$

$$\xi_{VO_2^+} = -N^{\mathrm{m}}_{V^{3+}} - 2N^{\mathrm{m}}_{V^{2+}} \quad [34b]$$

where the stoichiometric coefficients are obtained from the reaction mechanism given above. Again, the reaction between V^{2+} and VO_2^+ is not included in the model as it is redundant and yields the same species as those presented here.

Hydrogen and oxygen evolution reactions.—Hydrogen and oxygen evolution reactions are known to occur at the negative and positive electrodes when the corresponding overpotentials are sufficiently high. These reactions can be written in the form

$$2H^+ + 2e^- \longrightarrow H_2 \quad [35]$$

$$2H_2O \longrightarrow O_2 + 4H^+ + 4e^- \quad [36]$$

and tend to unbalance the battery by drifting the actual SOC of each electrolyte at different rates in a way that cannot be recovered by means of simple mixing strategies.[46,55–57]

The reaction kinetics are usually modeled using the Tafel equation assuming backward reactions are not favorable and reactants are present in excess at any moment[35,36]

$$i_{H_2} = -i_{0,H_2} \exp\left(-\frac{F\alpha_{H_2}\eta_{H_2}}{RT}\right) \quad [37a]$$

$$i_{O_2} = i_{0,O_2} \exp\left(\frac{F\alpha_{O_2}\eta_{O_2}}{RT}\right) \quad [37b]$$

where the overpotential for each reaction is $\eta_{H_2} = \phi_e - \phi_L - E^0_{H_2}$ and $\eta_{O_2} = \phi_e - \phi_L - E^0_{O_2}$. It is worth noting that in this model the electrolytes at the inlet of the working cell are assumed to be H_2- and O_2-free.

Boundary conditions.—A uniform electric potential is applied along the boundaries of the current collector applying a voltage difference V_{cell} between anode and the cathode. Electronic insulation boundary conditions are imposed in both faces of the membrane, which still allows ionic transport, while ionic insulation conditions are applied in both current collector surfaces. All remaining surfaces are assumed to be electrically insulated.

At both inlet sections, equilibrium concentrations of each ionic species are imposed following Eqs. 3, 9, 28 and 30. A uniform liquid velocity is specified at both half-cell inlets, computed from the

stipulated flow rates, Q_v, and the available cross-sectional area, W_eD_e, of the flow-through configuration. This yields a mean inlet velocity $u_{in} = Q_v/(W_eD_e)$ where W_e and D_e refer to the electrode width and depth in the x- and z-directions, respectively (see Fig. 1 and Table III). As the flow is incompressible, at the outlet Sections a uniform reference pressure $p_{out} = 0$ is prescribed for simplicity, so that the inlet pressure provides directly the pressure drop. For the remaining boundaries the species fluxes are set equal to zero. An sketch that summarizes the imposed boundary conditions is presented in Fig. 1b.

Results and Discussion

In this section, the unit-cell model proposed above is first validated against experimental measurements of OCV, electrolyte ionic conductivity and polarization curves at different operating conditions. Then, the model is used to explore the relevance of the various physico-chemical phenomena under study for different cell voltages, flow rates and SOCs.

Model validation.—Recent advances in the theoretical description of the different processes that occur in VRFBs have made it possible to improve the reliability of the first proposed models.[23,24] In particular, understanding the sensitivity to the model parameters can help to improve the description of the physics involved.[58] Here we have used the most advanced stationary VRFB models as starting point and introduced a few new descriptions of the physics in order to improve the accuracy of the numerical predictions.

As an illustrative example, Fig. 2a displays polarization curves that show the effect of including more and more rigorous descriptions of the different physical phenomena on the accuracy of the model predictions. Despite the order of inclusion (stated in the legend) is not relevant here, it gives an idea of the accuracy that can be obtained by refining the model. In that figure, the model reported by You et al.[24] is taken as a baseline being fed with the experimental parameters measured in this work. As can be seen, deviations in the cell voltage for each current density are controlled by different phenomena. The inclusion of experimental values of the electrochemical kinetic parameters of vanadium species on the carbon electrodes and the corrected equilibrium potential of the cell are critical to accurately represent the activation losses that dominate at low current densities. Sulfuric acid equilibrium reactions are important to estimate the species concentration, which have an important role in the ohmic losses controlled region of the polarization curve. The correction of electrolyte conductivity, by including proper local values of diffusion coefficients, directly affects the ohmic and mass transfer losses, explained by 5. Moreover, by thoroughly including local mass transfer coefficients in the model (Eq. 14) mass transfer losses can be better represented. Defining local values of electrolyte properties allows to avoid errors of roughly 10.5% when analyzing the current density response in the polarization curve (see Fig. S3). Finally, the inclusion of vanadium crossover corrects the ohmic resistance providing a more accurate prediction that adjusts to the experimental measurements. The only fitting parameter used in the model is the electrode specific surface area (see Table III), which is indeed a difficult parameter to determine experimentally. The final value of this parameter (2.3×10^4 m^2 m^{-3}) is similar to the value provided in the datasheet of the electrode manufacturer (3.6×10^4 m^2 m^{-3}).

Open circuit voltage.—Figure 2b compares the predicted OCV of the battery against experimental measurements and the most common Nernst expression for which a consistent difference of about 0.2 V is found for all SOCs. Solving Eqs. 28, 30 and 9 provides the equilibrium concentrations of H^+, HSO_4^-, SO_4^{2-} that can be used to calculate the equilibrium potential in the cell from Eq. 19. This alternative technique produces highly precise results that show only small differences (~20 mV) at high SOCs (>90%). A close examination of the results suggests that the deviations from the uncorrected Nernst expression are mostly due to the use of non-accurate standard reduction potentials, and the lack or incorrect inclusion of the proton concentration in the positive electrolyte and the Donnan potential in the membrane.

Electrolyte ionic conductivity.—Diffusion coefficients of vanadium species have a direct impact in the ionic conductivity of electrolytes. Most VRFB models use diffusion coefficients measured in electrolytes with compositions that differ to the simulated ones.[59] In this work, the diffusion coefficients of vanadium species are measured in the same electrolyte that is used in the battery at different SOCs (see Table I).

Figure 2c compares the ionic conductivity values obtained from our experimental results, the numerical values calculated using Eq. 11, and those calculated using the values of D_i reported by Yamammura et al.[59] where constant diffusion coefficients are assumed. This assumption leads to an overestimation of the electrolyte conductivity of one order of magnitude, which has a direct impact on the ohmic resistance of the battery. Experimental measurements show a higher conductivity for the positive electrolyte than the negative one. At the same time, an increase in the SOC leads to higher conductivity in both electrolytes. These experimental results are in agreement with.[60] The concentration of protons is higher in the positive electrolyte and increases in both cases with SOC as will be shown in Fig. 4 below. Protons have the highest mobility and an increase in its concentration is reflected in the conductivity of the electrolyte. All these trends are well represented by the proposed model.

Polarization and power density curves.—The electrochemical performance predicted by the model is validated using polarization measurements and their corresponding power densities at different flow rates and inlet SOCs. Figures 3a and 3b show the influence of the flow rate for two different SOCs, 20% and 60%. When the flow rate increases to 50 ml min^{-1}, an asymptotic behavior is observed in the cell performance. Above this flow rate, increasing even more the flow rate does not change the shape of the polarization curve. At such high flow rates, the transport of active species to the surface of the electrode is so fast that the overpotential due to this effect is negligible. Therefore, the battery is only controlled by activation (i.e., kinetic) and ohmic losses. Figures 3c and 3d illustrate the influence of SOC at two different flow rates, 12 and 30 ml min^{-1}. A gradual increment of the electrochemical performance of the battery is observed as the SOC grows, as expected for a discharge process. At 20% SOC, higher losses related to mass transfer are observed due to the low concentration of charged species available for reaction. Discrepancies between model and experiments are more remarkable at low cell voltages and close to the limiting current conditions, particularly for small SOCs and flow rates. However, this region of the polarization curve is where the experimental errors are larger due to the difficulty in maintaining stationary conditions (see Fig. S4).

H_2SO_4 equilibrium concentrations.—The equilibrium concentrations of sulfuric acid-related species (H^+, HSO_4^-, SO_4^{2-}) change with SOC. In particular, during cell operation the local concentrations of H^+ and vanadium ions change, shifting the bisulfate equilibrium and thus affecting the concentration of the rest of sulfuric acid-related species. In Fig. 4, the equilibrium concentration of all sulfuric acid-related species and vanadium ions obtained from solving Eqs. 28, 30 and 9 is presented for both electrolytes as a function of SOC. These results ignore species crossover in a first approximation. In both electrolytes, increasing SOC leads to higher concentrations of H^+ resulting from the production of protons in the positive half-cell, that also must partially cross the membrane to balance the total charge. As a result, HSO_4^- concentration increases and SO_4^{2-} decreases. The proton concentration of the positive electrolyte is approximately 1 M higher than that of the negative one. The range of H^+ concentration was corroborated with pH

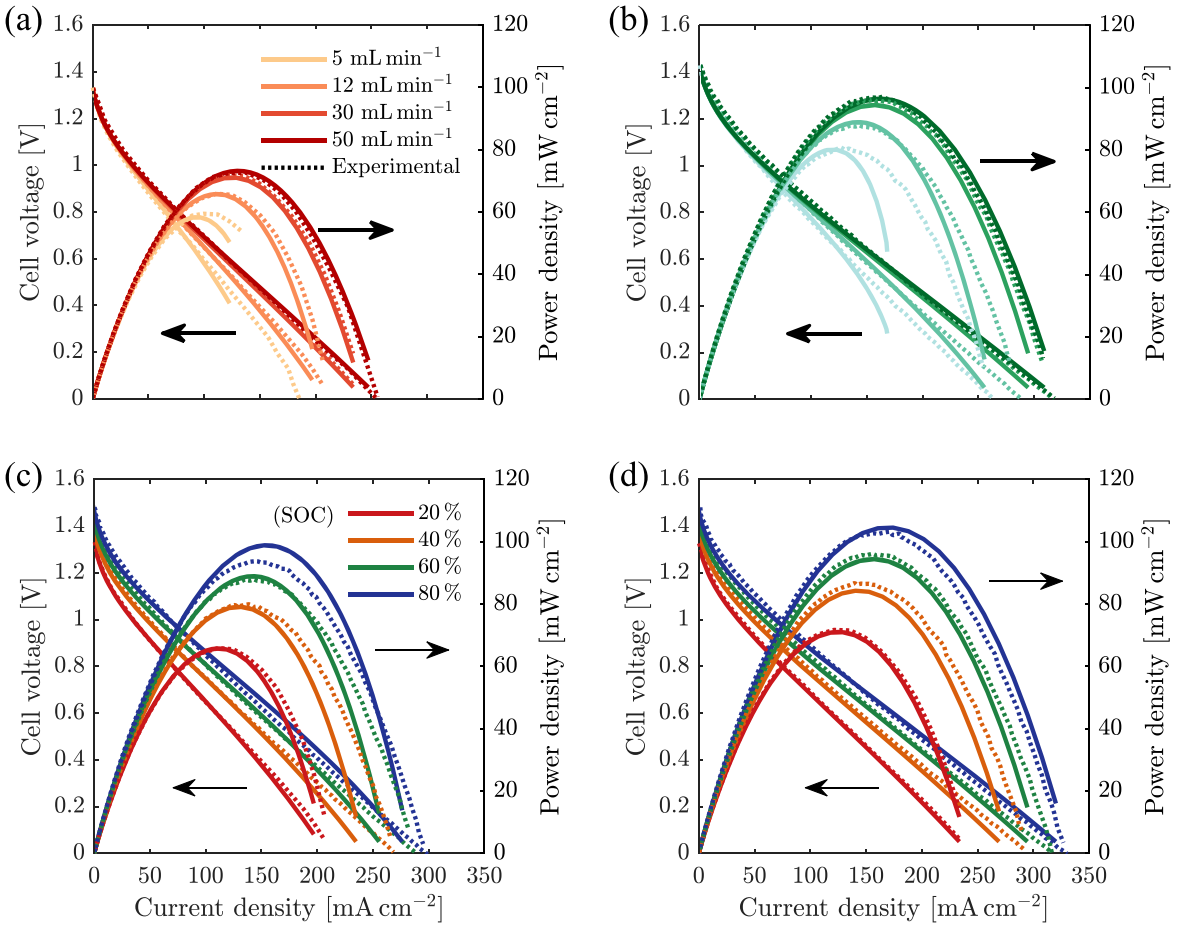

Figure 3. Experimental validation of the model using discharge polarization and power density curves at different flow rates for (a) 20% SOC and (b) 60% SOC; and at different SOCs for (c) 12 ml min^{-1} and (d) 30 ml min^{-1}.

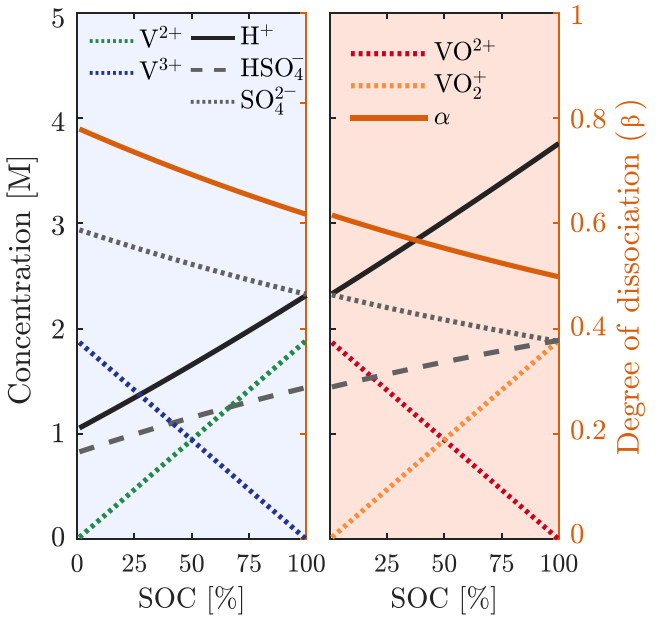

Figure 4. Equilibrium concentration of sulfate ions and vanadium species at different SOCs along with the degree of dissociation of HSO_4^- (β) in the negative (left) and positive (right) electrolytes.

measurements (see Table SI). All these results reveal that variations in the degree of dissociation (β, defined as the molal ratio of SO_4^{2-} to HSO_4^-) will occur, and those models that assume a constant value of β lead to inaccurate predictions of the H_2SO_4 equilibrium concentrations. Ion pairing has been reported between sulfate ions and vanadium species. This phenomena tend to increase the amount of dissociated acid in order to compensate for the deficiency of species.[61–64] However, this phenomena is not included in the model since there is no sufficient experimental works in the literature measuring this effect and therefore it is still unknown at which extend present molecules are paired.

Local mass transfer coefficients.—Spatial variations of the local mass transfer coefficients, $k_{m,j}$, can be also studied using the current model. Besides being coupled with the local current density given in Eq. 12a, mass transfer coefficients represent the inverse of a linear flux resistance, according to Eq. 13. Therefore, small values of $k_{m,j}$ are related with a slower transport of active species between the bulk fluid and the fiber surface. Local mass transfer coefficients thus give an idea of the effectiveness of diffusive transport in the pores in a certain region of the electrode, which is a valuable information that could be used to optimize future VRFB designs. In the proposed model, each vanadium species has its own local mass transfer coefficient so that highly specific transport information is generated.

Figure 5a shows contour plots of the dimensionless mass transport coefficients for the reduced species $j = \{V^{2+}, VO_2^+\}$ at representative operating conditions, namely 80% SOC, 50 ml min^{-1} and $V_{cell} = 1$ V. The averaged value shown on top of each subplot is used to non-dimensionalize the value of $k_{m,j}$. It is observed that mass transport is faster at the negative electrode, where it also experiences higher local variations. As described in Eq. 14, the mass transport coefficient depends on the electrolyte properties and on the diffusion

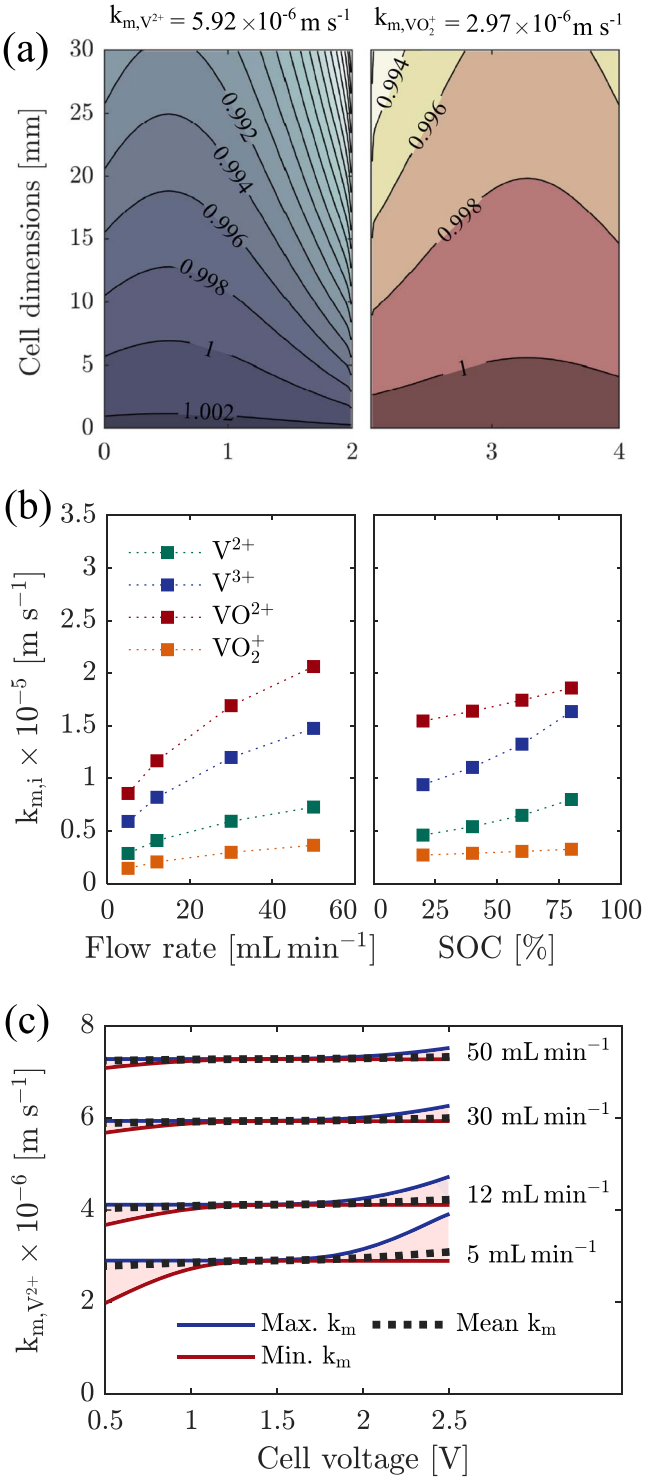

Figure 5. (a) Local mass transfer coefficient ($k_{m,j}$) for V^{2+} and VO_2^+ at 30 ml min^{-1} and 50% SOC, for $E_{cell} = 0.5$ V, in the negative and positive half-cells, respectively. (b) Averaged $k_{m,j}$ values of V^{2+} and VO_2^+ for different flow rates at 50% SOC (left) and different SOCs at 30 ml min^{-1} (right). (c) Minimum, maximum and averaged $k_{m,j}$ for V^{2+} at different cell potentials and flow rates.

coefficient of each vanadium ion, which is in turn function of the SOC. Regarding the effect of viscosity, since the negative electrolyte has a lower viscosity the ion diffusivities are higher, which results in higher mass transfer coefficients. Figure 5b shows that the mass transfer coefficients grow both with the volume flow rate and SOC. An overall dependence $k_m \propto u^{0.4}$ can be extracted from Eq. 14 that is reflected in the results. The reduction in viscosity is behind the general increasing trend of the mass transfer coefficients with SOC.

Finally, in Fig. 5c, the maximum, minimum and averaged values of k_m in the cell are analyzed at different cell potentials and flow rates, using V^{2+} as a representative case. High deviations, up to 30% above and below average at the lowest flow rates, appear in those regions where pore mass transport is a limiting factor. Large variations in local concentration due to the accumulation or scarcity of active species are responsible of this fluctuations that can be alleviated by increasing the flow rate. The large differences observed in the local mass transfer coefficients and the different trends they show with SOC justify the use of independent mass transport coefficients for the four vanadium ions.

Hydrogen parasitic evolution reactions.—Figure 6 presents the percentage of the applied current density that is being diverted to H_2 production in the negative half-cell. This parasitic evolution reaction is studied here at different SOCs and flow rates and for different operating cell voltages. Figure 6a reflects how higher flow rates can partially alleviate H_2 generation. Higher flow rates promote a flushing effect that disperse the charged molecules throughout the cell, thereby decreasing the local mass transfer concentration overpotential.[35,36] H_2 production is also represented for several inlet SOCs in Fig. 6b. As can be seen, increasing the SOC promotes H_2 generation. This is due to the higher overpotential which leads to higher electrochemical reaction rates for H_2. As it is observed from the results and also supported by other authors[35,36] even at low SOC, hydrogen evolution exists and must be considered during long-term operation as a source of electrolyte unbalance. While the SOC of the positive electrolyte will increase accordingly to the applied current, the SOC of the negative side will not increase as fast since part of the current will be diverted for H_2 generation. However, at realistic operating cell voltages, the electric current associated to this parasitic reaction is much smaller than the total current. Therefore, the consequences of hydrogen evolution cannot be seen in the charging polarization curves (see Fig. S5).

While efficiency and long-term capacity retention are affected, the most dangerous effect of H_2 parasitic reactions is the risk of bubble generation that clog the porous electrodes and cannot be easily redissolved. Figure 7 shows a risk map of bubbles evolution at different cell potentials and flow rates for two different SOCs. The presented risk is based on the proximity of the maximum H_2 concentration to its solubility limit (0.794 mol m^{-3} in water at 293 K and 1 atm). Similar maps can be used to guide operation of VRFBs avoiding H_2 generation. Furthermore, as previously reported by Shah et al.,[35] the region close to the cell outlet and membrane interface presents higher risk of bubbles evolution (see Fig. S7).

On the contrary, oxygen evolution is not as significant as hydrogen because the overpotential η_{O_2} is almost ten times lower than that for H_2.

Membrane crossover.—Long-term capacity fade of VRFBs is mostly caused by crossover of vanadium ions. The severity of crossover depends on the battery operating conditions. Here, we provide a detailed investigation of the crossover of the four vanadium ions analyzed at the membrane mid plane, $x = (x_1 + x_2)/2$, by calculating the area-averaged flux of each ionic species, N_i^m. Figures 8a–8d shows the flux of vanadium species lost (<0) by crossover toward the opposite half-cell at different cell voltages and operating conditions. Cell voltage is varied from discharge ($V_{cell} <$ OCV) to charge ($V_{cell} >$ OCV) cell potentials. As already reported by Oh et al.,[31] the crossover of negative species V^{2+}/V^{3+} dominates under discharge conditions, while that of positive species VO^{2+}/VO_2^+ is more significant under charge conditions.

In the proposed model, crossover fluxes of all species are composed by diffusion and migration contributions only, which are proportional to the diffusion coefficients in the membrane and to

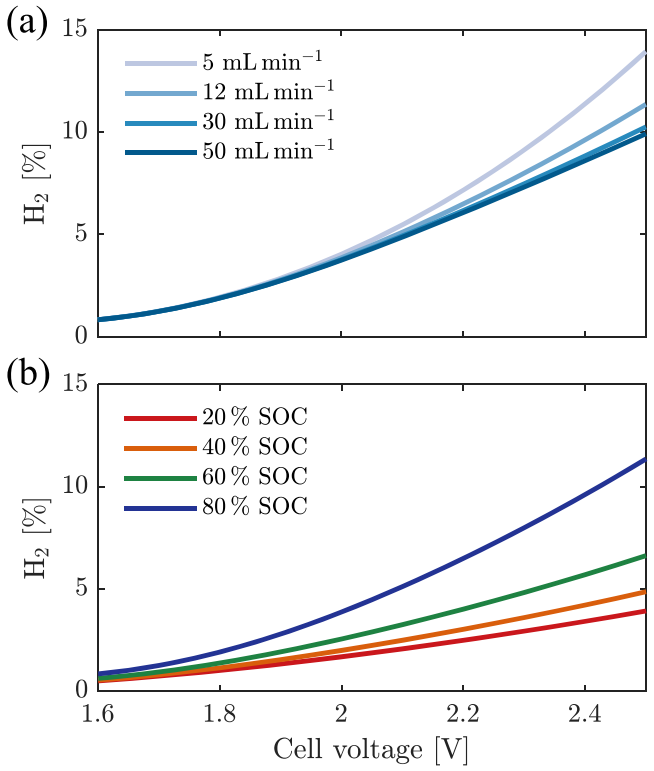

Figure 6. Variation of the percentage of current lost by H_2 evolution with the cell voltage for (a) various flow rates at 80% SOC, and (b) various SOCs at 12 ml min^{-1}.

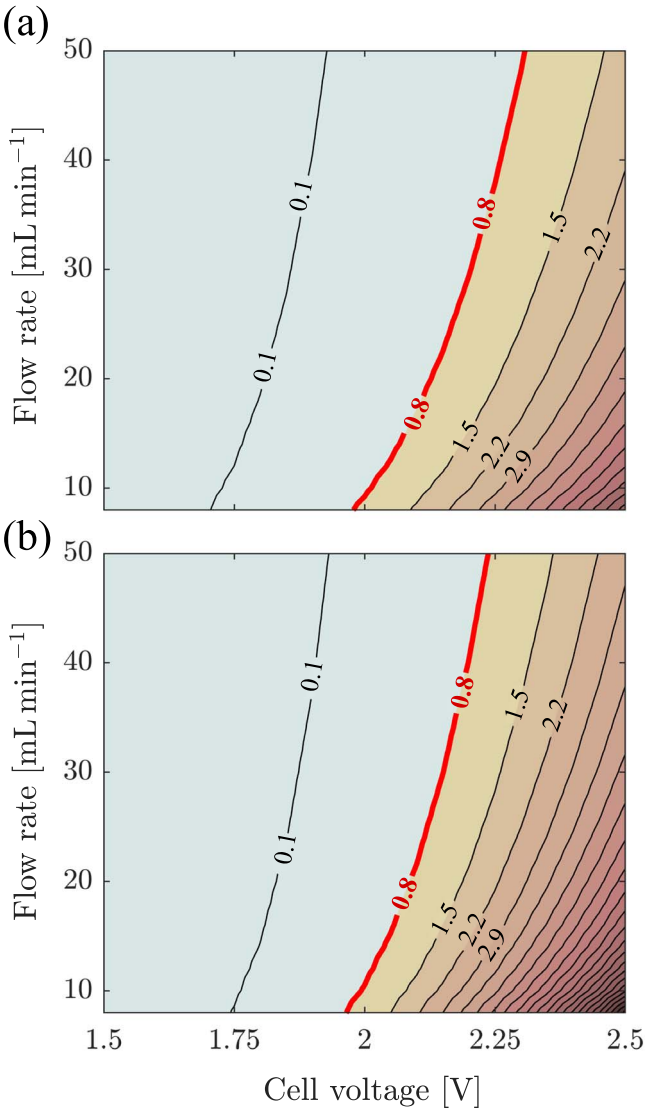

Figure 7. Concentration of dissolved H_2 and associated risk of bubble production (increasing from blue to red) for different cell voltages and flow rates at: (a) 20% SOC, and (b) 80% SOC.

the charge of each ion, respectively. The contribution of each transport mechanism (diffusion, migration and convection) on the crossover fluxes have been previously reported by other authors.[26,31,65] Despite not all transport mechanisms are not included in the computations, it is interesting to see the relative importance of the different transport mechanisms. Figure 8e shows the ratio between the diffusion and migration fluxes of all vanadium ions at different cell voltages. Diffusion is the dominating transport mechanism when the operating cell voltage is close to the OCV, due to the small current densities that prevail at these conditions. In fact, a vertical asymptote appears for $V_{cell} \approx$ OCV when the migration component vanishes. The diffusion to migration ratio is seen to change sign due to the change of the direction of the electric current vector. However, we have noticed that due to the potential discontinuity at the electrode-membrane interfaces caused by Donnan potential, an small electric field exist inside the membrane even for $V_{cell} =$ OCV that produce a shift of ≈160 mV on the value at which the migration component becomes zero (location of the asymptote).

At extreme values of V_{cell} both diffusion and migration are equally relevant and their flux ratio tends to unity. However, diffusion becomes negligible for the negative species (V^{2+} and V^{3+}) at discharge potentials, and similarly, for positive species (VO^{2+} and VO_2^+) at charge potentials, so that this ratio is close to zero instead. This unexpected behavior can be explained by analysing the concentration profiles of vanadium ions within the membrane at different cell voltages.[66] At discharge potentials, the membrane is flooded with V^{2+} and V^{3+} (see Fig. 9a) and no significant concentration gradient is observed at the membrane mid-plane, which results in a decreased value of the diffusion flux of these species. In that situation, self-discharge reactions are present almost completely at the positive electrolyte side of the membrane which produces a characteristic peak in the concentration of VO^{2+} and VO_2^+. The opposite situation is observed when the electric current is reverted. Additionally, the different charges of vanadium species generate a small asymmetry on the distribution of both transport mechanism that is barely noticeable in Fig. 8e.

The influence of flow rate on the crossover fluxes is represented in Figs. 8a and 8c. Species generated by charge or discharge of the battery tend to accumulate in the electrode at low flow rates and therefore, crossover is increased due to an enhanced concentration gradient across the membrane. On the other hand, consumed species are scarce near the outlet Section at lower flow rates, which in turn decreases the crossover flux of those species. An apparent exception to this behavior can be seen for the the case of V^{2+} for which crossover varies in only a small amount. It is important to note that crossover variations for different flow rates are a complex length-wise effect that cannot be studied by analysing each perpendicular Section independently, which highlights the utility of two-dimensional models. An easier interpretation of the results can be provided for the case of increasing inlet SOC. Higher concentration of the studied vanadium species always produce a greater crossover flux due to an accentuated concentration gradient, as can be seen in Figs. 8b and 8d.

Net fluxes: self-discharge effect.—All vanadium species that cross the membrane will unavoidably react with those present in the

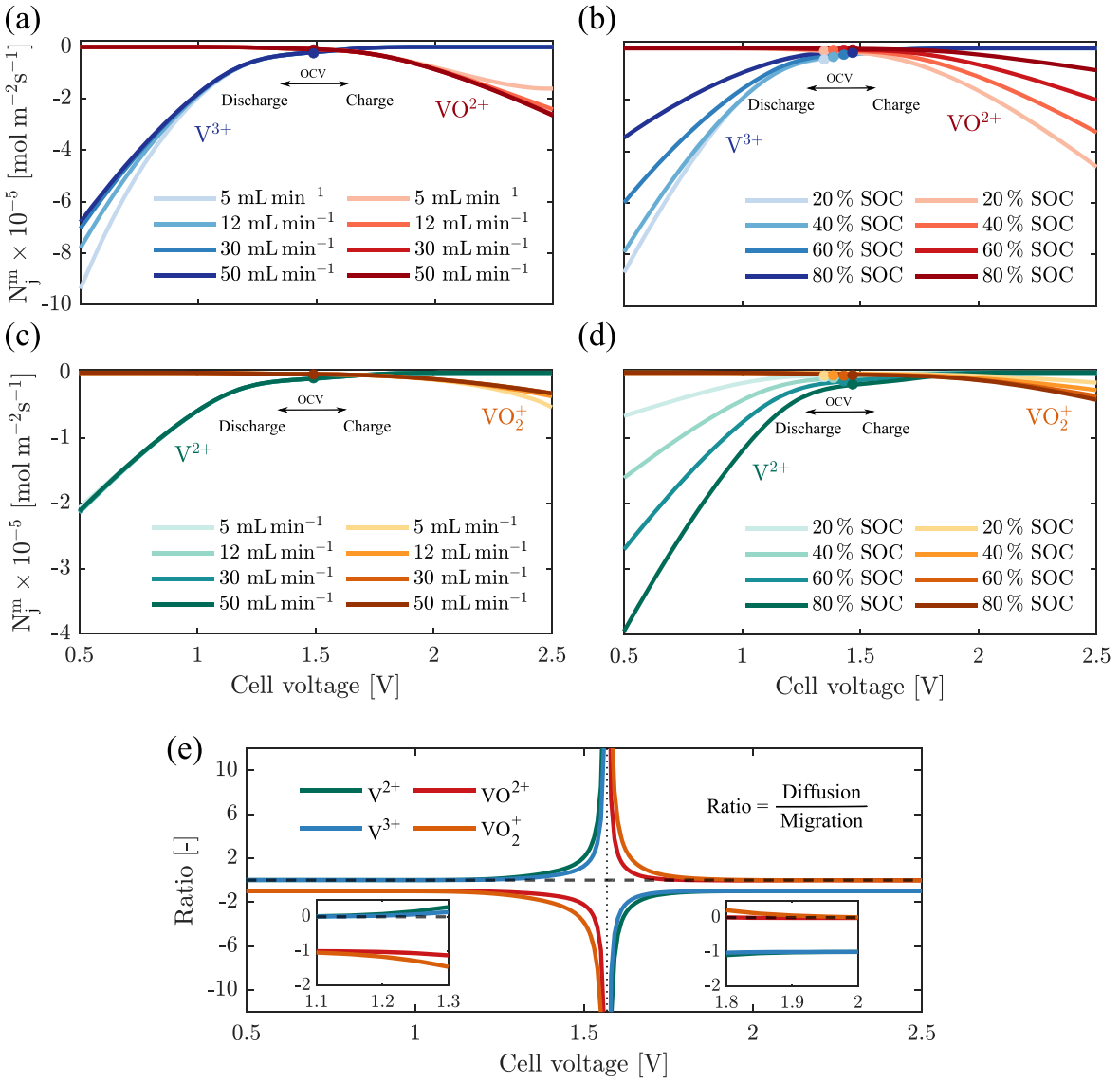

Figure 8. Crossover fluxes at different cell voltage of (a) V^{3+} and VO^{2+} and (c) V^{2+} and VO_2^+ for different flow rates at 50% SOC and of (b) V^{3+} and VO^{2+} and (d) V^{2+} and VO_2^+ for different SOCs at 30 ml min^{-1}; (e) ratio between diffusion and migration fluxes for all vanadium species at different cell voltages at 50% SOC and 30 ml min^{-1}. Filled colored points represent the OCV values at each operating SOC.

opposite half-cell according to the self-discharged reactions that occur in the electrolyte bulk (reactions 31 and 33). These side reactions are fast and irreversible and reduce the cell capacity and the coulombic efficiency.[32,52,54] According to the reaction mechanism, charged species (V^{2+} and VO_2^+) that cross the membrane are fully consumed, while discharged species (V^{3+} and VO^{2+}) are generated. Here, an average net flux term Ψ_j is defined for each vanadium species j to account for the species lost (<0) or gained (>0) in their respective half-cells as a result of the combination of crossover and self-discharged reactions.[54]

Figure 9a shows the concentration profiles of vanadium species across the membrane at the center of the reaction cell ($y = L/2$) for 30 ml min^{-1}, 50% SOC and $V_{cell} = 1$ V. Vanadium ions coming from one of the half-cells are fully consumed by self-discharge reactions in the opposite electrode-membrane interface. These results exhibit similar trends and non-linear species concentration profiles as in Yang et al.,[20] despite we have not included the convective transport through the membrane. Figure 9b shows the net flux of total vanadium species in each electrolyte as a function of the cell voltage for the same flow rate and SOC mentioned above, together with the SOC variation (ΔSOC) across the cell due to these net fluxes only. Here, the effect of the parasitic reactions is subtracted so that the isolated effect of crossover and self-discharge is studied. At discharge cell potentials, the net flux of total vanadium species of both electrolytes presents higher variations than under charge conditions. Opposite trends are observed between the positive and negative electrolytes as the sum of their net fluxes must remain equal to zero. The cumulative effect of total vanadium fluxes, also found in the works of,[32,65] explains why Sun et al.[51] reported experiments with decreasing and increasing concentrations of total vanadium species for the positive and negative electrolyte, respectively, over the long-term cycling of the battery. A detailed inspection of Fig. 9b reveals a significant decrease in SOC for the positive electrolyte during discharge, and for the negative electrolyte during charge. The cutoff potentials selected during charge-discharge cycles will therefore affect the severity of the capacity decay due to the asymmetry of fluxes. Unexpected positive values of ΔSOC can be easily explained as the flux of total vanadium, appearing in the denominator of Eq. 3, is greater than the flux of charged species. These results may give a false idea that the battery

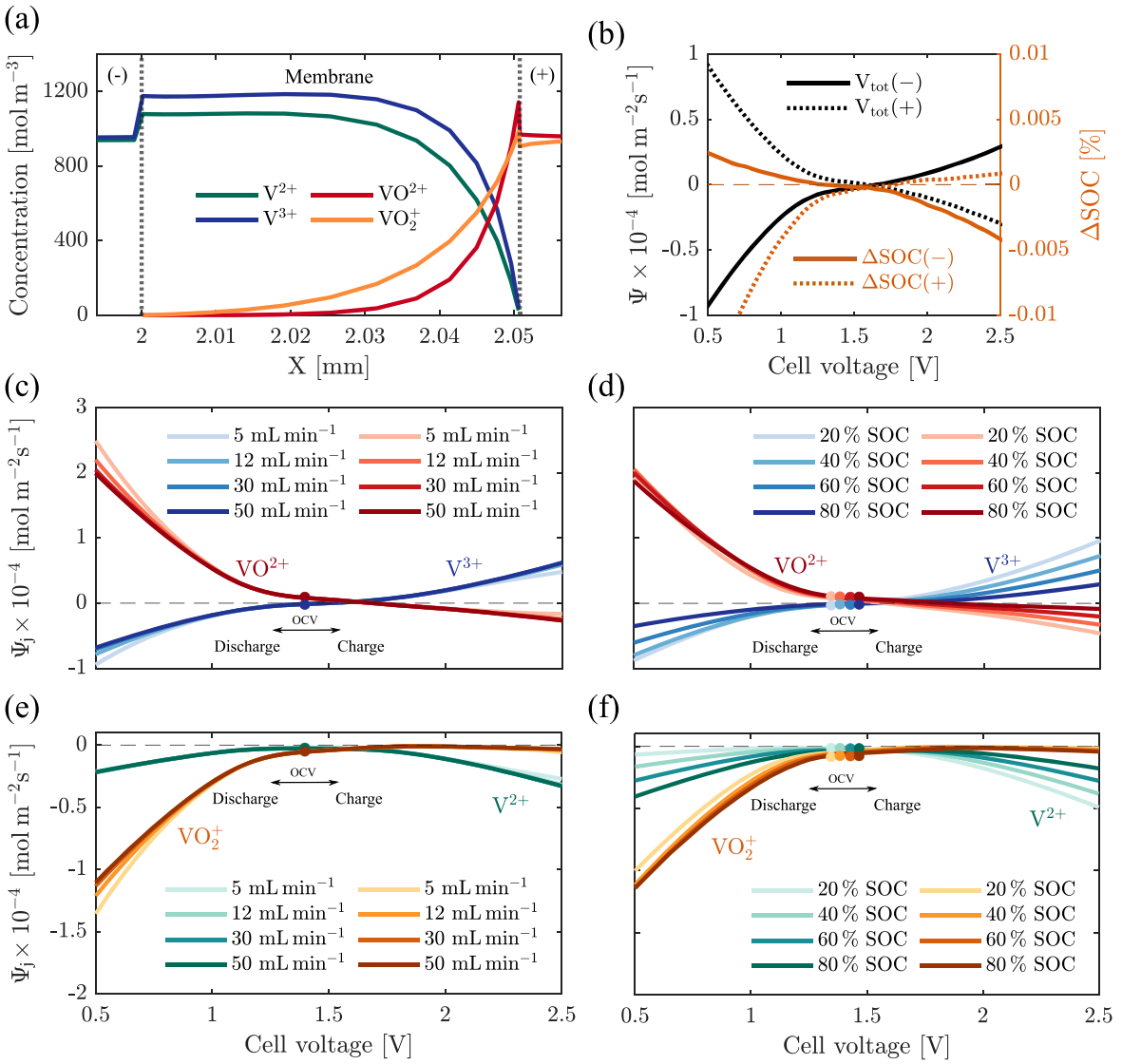

Figure 9. (a) Concentration of vanadium ions across the membrane at 30 ml min^{-1}, 50% SOC and $V_{cell} = 1$ V and (b) net flux of total vanadium at the same conditions together with SOC increment across the reaction cell for both electrolytes; Net flux of V^{3+} and VO^{2+} for different (c) flow rates at 50% SOC; and (d) SOC at 30 ml min^{-1}; V^{3+} and VO^{2+} for different (e) flow rates at 50% SOC; and (f) SOC at 30 ml min^{-1}. The filled colored points represent the OCV values for certain operating SOC.

is partially charging due to crossover, however, the capacity of the battery will always fade when the total amount of vanadium ions in one of the electrolytes decreases.[28,67,68]

For the positive electrolyte, the SOC always decreases over the cycles since the increment of ΔSOC is almost negligible during charge compared with the ΔSOC decay at discharge. However, for the negative electrolyte, it highly depends on the voltage chosen. These results may explain why some studies report decreasing SOC values in the negative electrolyte over the charge-discharge cycles.[67]

Figures 9c-f show the variation of the net flux of the four vanadium ions with the cell voltage for fixed SOC and different flow rates, and *vice versa*. Charged species, V^{2+} and VO_2^+, suffer negative net fluxes for all cell voltages due to their consumption by self-discharge reactions. On the contrary, V^{3+} experiences a positive net flux at charge potentials due to the significant production from self-discharge reactions and almost zero crossover. The same occurs for VO^{2+} at discharge cell potentials. In Figs. 9c and 9e, the influence of the flow rate on the net flux of vanadium ions is shown. Its contribution to self-discharge is only significant at high current densities for which pore mass transport is the limiting factor and local concentrations of active species suffer the greatest variations. In general, for discharged species, it can be seen that under discharge conditions higher flow rates alleviate self-discharge. However, during charge, the flow rate has an opposite impact. These trends are in line with crossover results presented before. Finally, in panels d and f of Fig. 9 the influence of SOC is analyzed. Increasing SOC the net flux of discharged species is reduced due to its scarcity. An unexpected effect is produced during charge for which an increase in SOC yields lower VO_2^+ losses. A negligible crossover flux of VO_2^+ accompanied by a decreasing flux of VO^{2+} for higher values of SOC explains that trend.

Conclusions

In this work, an advanced 2D steady-state isothermal model of a unit cell all-vanadium redox flow battery has been presented. The model is based on recent state-of-art models and includes for the first time a complete description of H_2SO_4 dissociation reactions and local mass transfer coefficients for all vanadium species. The resulting model is fed with measured electrochemical kinetic and electrolyte properties and validated at different SOCs and flow rates using polarization, open circuit voltage and electrolyte conductivity

measurements at a constant system temperature of 25 °C, using the electrode specific surface area as the only fitting parameter. Predicted conductivity and OCV values agree fairly well with experiments. However, model predictions are less accurate at limited reactant conditions (low SOCs and flow rate) and high electric currents, where parasitic H_2 and O_2 evolution reactions are known to occur. This discrepancies are also related to significant experimental errors. Following the validation of the model, a set of parametric sweeps provided numerical results that were used to reveal the role of operating conditions (SOC, flow rate and cell voltage) on the main parasitic phenomena affecting the operation of VRFBs, namely vanadium crossover, self discharge reactions and gas evolution.

Equilibrium concentrations, calculated as part of the solution, present great deviations in the degree of dissociation of HSO_4^- for different SOCs, which justifies the use of an equilibrium reaction constant to model sulfuric species and proton concentrations instead of a constant degree of dissociation. Large local deviations of the mass transfer coefficients both spatially and among different vanadium species justify the use of local values and different coefficients for the different species to model pore mass transport. Maps of the risk of H_2 bubble production as a function of different operation conditions are supplied and an increase on the flow rate is proposed as a means to retard the onset of bubble production. Significant crossover of negative-electrolyte species must be considered during discharge while positive-electrolyte species tend to cross during charge. When self-discharge reactions are included the net flux of charged species lost is always negative but unequal during the charge and discharge modes. The net flux of total vanadium species of each electrolyte is greater for discharge conditions. The single-pass SOC variation in the positive and negative electrodes has been represented as a function of the cell voltage, showing that self-discharge reactions and crossover contribute greatly to the unbalance and capacity decay of the battery.

Overall, we provide a reliable steady-state model validated with multitude of experiments that will be used to study battery stacks and to optimize larger systems and provide operation guidelines. The advanced state-of-the-art model presented herein is a first step toward a more complex accurate dynamic model that can perform predictions at system level.

Acknowledgments

This work has been partially funded by the Agencia Estatal de Investigación (PID2019-106740RB-I00 and RTC-2017-5955-3/AEI/10.13039/501100011033). Dr. García-Salaberri also acnowledges the support of the projects EIN2020-112247 (Spanish Agencia Estatal de Investigación). The authors want to acknowledge Maxime van der Heijden for her critical feedback.

ORCID

Vanesa Muñoz-Perales https://orcid.org/0000-0002-9691-918X
Enrique García-Quismondo https://orcid.org/0000-0002-7939-9573
Pablo A. García-Salaberri https://orcid.org/0000-0002-3918-5415
Jesús Palma https://orcid.org/0000-0003-1022-0165
Marcos Vera https://orcid.org/0000-0001-6878-1788
Santiago E. Ibáñez https://orcid.org/0000-0001-5114-2226

References

1. B. R. Chalamala, T. Soundappan, G. R. Fisher, M. R. Anstey, V. V. Viswanathan, and M. L. Perry, *Proc. IEEE*, **102**, 976 (2014).
2. A. Dehghani-Sanij, E. Tharumalingam, M. Dusseault, and R. Fraser, *Renew. Sustain. Energy Rev.*, **104**, 192 (2019).
3. S. Koohi-Fayegh and M. Rosen, *Journal of Energy Storage*, **27**, 101 (2020).
4. E. Sánchez-Díez, E. Ventosa, M. Guarnieri, A. Trovó, C. Flox, R. Marcilla, F. Soavi, P. Mazur, E. Aranzabe, and R. Ferret, *J. Power Sources*, **481**, 228 (2021).
5. W. Wang, Q. Luo, B. Li, X. Wei, L. Li, and Z. Yang, *Adv. Funct. Mater.*, **23**, 970 (2013).
6. X. Zhou, X. Zhang, L. Mo, X. Zhou, and Q. Wu, *Small*, **16**, 1 (2020).
7. X. Zhou, X. Zhang, Y. Lv, L. Lin, and Q. Wu, *Carbon*, **153**, 674 (2019).
8. C. T. Wan, R. R. Jacquemond, Y. Chiang, K. Nijmeijer, F. R. Brushett, and A. Forner-Cuenca, *Adv. Mater.*, **33**, 2 (2021).
9. T. N. L. Doan, T. K. A. Hoang, and P. Chen, *RSC Adv.*, **5**, 72805 (2015).
10. B. G. Thiam and S. Vaudreuil, *J. Electrochem. Soc.*, **168**, 070553 (2021).
11. B. Akuzum, Y. C. Alparslan, N. C. Robinson, E. Agar, and E. C. Kumbur, *J Appl Electrochem*, **49**, 551 (2019).
12. Y. Zeng, F. Li, F. Lu, X. Zhou, Y. Yuan, X. Cao, and B. Xiang, *Appl. Energ.*, **238**, 435 (2019).
13. D. Aaron, Z. Tang, A. B. Papandrew, and T. A. Zawodzinski, *J. Appl. Electrochem.*, **41**, 1175 (2011).
14. R. Schweiss, C. Meiser, and D. Dan, *Batteries*, **4**, 55 (2018).
15. B. Xiong, J. Zhao, and J. Li, *2013 IEEE Power & Energy Society General Meeting, IEEE* 1 (2013).
16. M. van der Heijden, R. van Gorp, M. Sadeghi, J. Gostick, and A. Forner-Cuenca, *J. Electrochem. Soc.*, **169**, 040505 (2022).
17. M. Sadeghi, M. Aganou, M. Kok, M. Aghighi, G. Merle, J. Barralet, and J. Gostick, *J. Electrochem. Soc.*, **166**, A2121–30 (2019).
18. X. Ma, H. Zhang, and F. Xing, *Electrochim. Acta*, **58**, 238 (2011).
19. Q. Zheng, X. Li, Y. Cheng, G. Ning, F. Xing, and H. Zhang, *Appl. Energ.*, **132**, 254 (2014).
20. W. Yang, Y. He, and Y. Li, *Electrochim. Acta*, **155**, 279 (2015).
21. Q. Xu and T. Zhao, *Prog. Energ. Combust.*, **49**, 40 (2015).
22. A. Weber, M. Mench, J. Meyers, P. Ross, J. Gostick, and Q. Liu, *J. Appl. Electrochem.*, **41**, 1137 (2011).
23. A. Shah, M. Watt-Smith, and F. Walsh, *Electrochim. Acta*, **53**, 8087 (2008).
24. D. You, H. Zhang, and J. Chen, *Electrochim. Acta*, **54**, 6827 (2009).
25. H. Al-Fetlawi, A. Shah, and F. Walsh, *Electrochim. Acta*, **55**, 78 (2009).
26. K. W. Knehr, E. Agar, C. R. Dennison, A. R. Kalidindi, and E. C. Kumbur, *J. Electrochem. Soc.*, **159**, A1446 (2012).
27. K. Oh, H. Yoo, J. Ko, S. Won, and H. Ju, *Energy*, **81**, 3 (2015).
28. M. Y. Lu, W. W. Yang, X. S. Bai, Y. M. Deng, and Y. L. He, *Electrochim. Acta*, **319**, 210 (2019).
29. K. Knehr and E. Kumbur, *Electrochem. Commun.*, **13**, 342 (2011).
30. A. Tang, J. Bao, and M. Skyllas-Kazacos, *J. Power Sources*, **196**, 10737 (2011).
31. K. Oh, S. Won, and H. Ju, *Electrochim. Acta*, **181**, 238 (2015).
32. L. Hao, Y. Wang, and Y. He, *J. Electrochem. Soc.*, **166**, A1310 (2019).
33. Q. Xu, T. Zhao, and C. Zhang, *Appl. Energ.*, **130**, 139 (2014).
34. X. Zhou, T. Zhao, L. An, Y. Zeng, and X. Yan, *Appl. Energ.*, **158**, 157 (2015).
35. A. Shah, H. Al-Fetlawi, and F. Walsh, *Electrochim. Acta*, **55**, 1125 (2010).
36. H. Al-Fetlawi, A. Shah, and F. Walsh, *Electrochim. Acta*, **55**, 3192 (2010).
37. S. K. Murthy, A. K. Sharma, C. Choo, and E. Birgersson, *J. Electrochem. Soc.*, **165**, A1746 (2018).
38. Y. A. Gandomi, D. S. Aaron, T. A. Zawodzinski, and M. M. Mench, *J. Electrochem. Soc.*, **163**, A5188 (2016).
39. S. Tsushima and T. Suzuki, *J. Electrochem. Soc.*, **167**, 020553 (2020).
40. Q. Ma, L. Xing, H. Su, W. Zhang, W. Yang, and Q. Xu, *Chem. Eng. J.*, **393**, 124753 (2020).
41. D. Krishnamurthy, E. O. Johansson, J. W. Lee, and E. Kjeang, *J. Power Sources*, **196**, 10019 (2011).
42. Q. Xu and T. Zhao, *Phys. Chem. Chem. Phys.*, **15**, 10841 (2013).
43. L. Xia, W. Huo, H. Zhang, K. Xu, Y. Qing, F. Chu, C. Zou, H. Liu, and Z. Tan, *ACS Appl. Energy Mater.*, **5**, 1984 (2022).
44. D. A. Knopf, B. P. Luo, U. K. Krieger, and T. Koop, *J. Phys. Chem. A*, **107**, 4322 (2003).
45. E. Agar, C. Dennison, K. Knehr, and E. Kumbur, *J. Power Sources*, **225**, 89 (2013).
46. M. M. Saleh and J. Solid, *State Electr.*, **11**, 811 (2007).
47. Y. Lee, S. Kim, R. Hempelmann, J. H. Jang, H. J. Kim, J. Han, J. Kim, and D. Henkensmeier, *J. Appl. Polym. Sci.*, **136**, 47547 (2019).
48. L. Eifert, R. Banerjee, Z. Jusys, and R. Zeis, *J. Electrochem. Soc.*, **165**, A2577 (2018).
49. E. L. B. Bird and W. Stewart, *Transport Phenomena* (Wiley, NY) (2002).
50. M. A. Aziz and S. Shanmugam, *J. Mater. Chem. A*, **6**, 17740 (2018).
51. C. Sun, J. Chen, H. Zhang, X. Han, and Q. Luo, *J. Power Sources*, **195**, 890 (2010).
52. M. Skyllas-Kazacos and M. Kazacos, *J. Power Sources*, **196**, 8822 (2011).
53. Z. Jiang, K. Klyukin, K. Miller, and V. Alexandrov, *The Journal of Physical Chemistry B*, **123**, 3976 (2019).
54. S. E. Ibáñez, A. E. Quintero, P. A. García-Salaberri, and M. Vera, *Int. J. Heat Mass Tran.*, **170**, 121022 (2021).
55. A. Fetyan, G. A. El-Nagar, I. Lauermann, M. Schnucklake, J. Schneider, and C. Roth, *J. Energy Chem.*, **32**, 57 (2019).
56. C. N. Sun, F. M. Delnick, L. Baggetto, G. M. Veith, and T. A. Zawodzinski, *J. Power Sources*, **248**, 560 (2014).
57. L. Wei, T. Zhao, Q. Xu, X. Zhou, and Z. Zhang, *Appl. Energ.*, **190**, 1112 (2017).
58. Y. Y. Choi, S. Kim, S. Kim, and J. I. Choi, *J. Power Sources*, **450**, 227684 (2020).
59. T. Yamamura, N. Watanabe, T. Yano, and Y. Shiokawa, *J. Electrochem. Soc.*, **152**, A830 (2005).
60. M. Skyllas-Kazacos, L. Cao, M. Kazacos, N. Kausar, and A. Mousa, *ChemSusChem*, **9**, 1521 (2016).
61. S. D. Zhang, P. H. Ma, Y. C. Zhai, and W. M. Chen, *Rare Metals*, **34**, 873 (2015).
62. M. Asem, *Ph.D. dissertation*, University of New South Wales (2003).
63. L. Xiang-Rong, Q. Ye, X. Wei-Guo, L. Jian-Guo, Y. Jia-Zhen, X. Qian, and Y. Chuan-Wei, *J. Solution Chem.*, **45**, 1879 (2016).
64. G. Oriji, Y. Katayama, and T. Miura, *Electrochim. Acta*, **49**, 3091 (2004).
65. E. Agar, K. Knehr, D. Chen, M. Hickner, and E. Kumbur, *Electrochim. Acta*, **98**, 66 (2013).
66. X. G. Yang, Q. Ye, P. Cheng, and T. S. Zhao, "Effects of the electric field on ion crossover in vanadium redox flow batteries." *Applied Energy*, **145**, 306 (2015).
67. Q. Luo, L. Li, W. Wang, Z. Nie, X. Wei, B. Li, B. Chen, Z. Yang, and V. Sprenkle, *ChemSusChem*, **6**, 268 (2013).
68. B. Jiang, L. Wu, L. Yu, X. Qiu, and J. Xi, *J. Membrane Sci.*, **510**, 18 (2016).